



HAL
open science

Hydration of Na-saturated Synthetic Stevensite, a Peculiar Trioctahedral Smectite

Doriana Vinci, Martine Lanson, Valérie Magnin, Nathaniel Findling, Bruno Lanson

► **To cite this version:**

Doriana Vinci, Martine Lanson, Valérie Magnin, Nathaniel Findling, Bruno Lanson. Hydration of Na-saturated Synthetic Stevensite, a Peculiar Trioctahedral Smectite. Clay Minerals, 2020, 10.1180/clm.2020.32 . insu-03022632

HAL Id: insu-03022632

<https://insu.hal.science/insu-03022632>

Submitted on 25 Nov 2020

HAL is a multi-disciplinary open access archive for the deposit and dissemination of scientific research documents, whether they are published or not. The documents may come from teaching and research institutions in France or abroad, or from public or private research centers.

L'archive ouverte pluridisciplinaire **HAL**, est destinée au dépôt et à la diffusion de documents scientifiques de niveau recherche, publiés ou non, émanant des établissements d'enseignement et de recherche français ou étrangers, des laboratoires publics ou privés.

1 Hydration of Na-saturated Synthetic Stevensite, a Peculiar Trioctahedral Smectite

2

3 Doriana Vinci^{1,2}, Bruno Lanson^{1,*}, Martine Lanson¹, Valérie Magnin¹, Nathaniel Findling¹

4

5 *Univ. Grenoble Alpes, Univ. Savoie Mont Blanc, CNRS, IRD, Univ. Gustave Eiffel, ISTerre, F-*
6 *38000 Grenoble, France*

7 *Dipartimento Scienze Terra & Geoambientali, Univ. Bari Aldo Moro, Bari, Italy*

8

9 Running title: Hydration of Na-saturated Synthetic Stevensite

10

11 *. Corresponding author: bruno.lanson@univ-grenoble-alpes.fr

12

13 **Abstract**

14 Smectite interlayer water plays a key role on the mobility of elements and molecules, but also
15 in a variety of geological processes. In contrast to saponite and hectorite, whose layer charge
16 originates from isomorphous substitutions, stevensite layer charge originates from the presence
17 of octahedral vacancies. Despite its common occurrence in lacustrine environments, hectorite
18 hydration has received little attention, compared to saponite and hectorite. Early reports
19 mention a specific hydration behavior, however, with the systematic presence of a low-angle
20 reflection attributed to the regular interstratification of different hydration states. The
21 present study aims at revisiting this specific hydration behavior in more depth. Within this
22 scope, the hydration behavior of the above three smectite varieties are compared using
23 synthetic trioctahedral smectites of similar layer charge, and different compositions of their
24 octahedral sheets. The chemical composition of the octahedral sheet does not appear to
25 influence significantly smectite hydration for saponite and hectorite. Compared to its saponite
26 and hectorite equivalents, H₂O content in stevensite is lower by ~2.0 mmol H₂O per g of dry
27 clay. Consistent with this lower H₂O content, Zn-stevensite lacks a stable monohydrated state,
28 dehydrated layers prevailing from 60 to 0% RH. The presence of the regular interstratification
29 of 0W and 1W layers is responsible for the low-angle reflection commonly observed for
30 stevensite under air-dried conditions. Finally, stevensite identification method based on X-ray
31 diffraction of heated and EG-solvated samples is challenged by the strong influence of
32 octahedral sheet chemical composition (Zn or Mg in the present study) on hectorite swelling
33 behavior. The origin of this effect remains undetermined and further work is needed to
34 propose a more general identification method.

35

36 **Keywords:** Smectite hydration, stevensite, smectite identification

37 Introduction

38 Smectites are phyllosilicates whose 2:1 layers consist of two tetrahedral sheets sandwiching
39 an octahedral one. In trioctahedral smectites the three octahedral sites are all occupied by
40 divalent cations, usually Mg^{2+} . Isomorphic substitutions occurring either in tetrahedral or in
41 octahedral sheets (Al-for-Si and Li-for-Mg, respectively) or the presence of vacant octahedral
42 sites induce a layer charge deficit which is compensated for by the presence of hydrated
43 exchangeable cations within smectite interlayers and at the mineral surface. Based on the
44 origin of the layer charge deficit, trioctahedral smectites have received different mineral
45 names: saponite, hectorite, and stevensite for tetrahedral substitutions, octahedral
46 substitutions and octahedral vacancies, respectively (Brindley, 1980). Following the
47 pioneering works of Nagelschmidt (1936) and Bradley *et al.* (1937), smectite hydration has
48 drawn a lot of attention, owing to the key influence played by smectite interlayer water on
49 the mobility of contaminants and nutrients (Laird *et al.*, 1991), but also in a variety of
50 geological settings (See Ferrage *et al.*, 2010, and references therein). The influence of the
51 amount and location of isomorphic substitutions on trioctahedral smectite (saponite and
52 hectorite) hydration has been extensively investigated over the last decade or so (Ferrage *et al.*,
53 2005a, 2010, 2011; Malikova *et al.*, 2005, 2007; Michot *et al.*, 2005, 2007, 2012; Rinnert *et al.*,
54 2005; Dazas *et al.*, 2015; Vinci *et al.*, 2020). This interest has been sustained by the frequent
55 use of smectite in natural and engineered barriers in (nuclear) waste repositories and by the
56 related requirements for their safety assessment. In both saponite and hectorite, the presence
57 of discrete hydration states similar to those reported in the pioneering works on smectite
58 hydration (Bradley *et al.*, 1937; Mooney *et al.*, 1952; Norrish, 1954b) leads to the well-known
59 stepwise expansion of the layer-to-layer distance. With increasing water activity, the
60 occurrence of dehydrated layers (0W, $d_{001} = 9.6\text{--}10.2 \text{ \AA}$) is followed by 1W, 2W, and 3W
61 hydration states ($d_{001} = 11.6\text{--}12.9 \text{ \AA}$, $d_{001} = 14.9\text{--}15.7 \text{ \AA}$, $d_{001} = 18\text{--}19 \text{ \AA}$, respectively),
62 corresponding to the intercalation of 1, 2, and, less frequently, 3 “planes” of interlayer H_2O
63 molecules.

64 Stevensite, whose layer charge deficit originates from the presence of octahedral
65 vacancies, is a common smectite in lacustrine environments (Eberl *et al.*, 1982; Khoury *et al.*,
66 1982; Jones, 1986; Thiry *et al.*, 2014; Bentz and Peterson, 2020; De Oliveira Nardi Leite *et al.*,
67 2020) By contrast, hydration of stevensite, whose layer charge deficit originates from the

68 presence of octahedral vacancies. Compared to saponite and hectorite, its hydration has
69 received much less attention although early reports mention a very specific behavior
70 (Brindley, 1955; Faust *et al.*, 1959; Shimoda, 1971). In particular, these studies systematically
71 mention the occurrence of a low-angle reflection tentatively assigned to the regular
72 alternation of OW and 2W layers (Brindley, 1955). The present study thus aims at revisiting
73 this peculiar hydration behavior in more depth. For this purpose, two stevensite samples, with
74 Zn- and Mg-rich octahedral sheets, were hydrothermally synthesized together with their
75 saponite and hectorite chemical equivalents. All synthesized samples have similar layer charge
76 deficits of $\sim 0.8 e^-$ per $O_{20}(OH)_4$. Hydration of all samples was systematically assessed using
77 volumetric H_2O vapor (de)sorption isotherms and X-ray diffraction under controlled humidity
78 conditions. Quantitative profile fitting of X-ray diffraction data was used both to assess the
79 relative proportions of the different hydrates and the evolution of these proportions as a
80 function of H_2O activity, and to unravel the origin of the low-angle reflection, if any.

81

82 **Materials and methods**

83 *Sample preparation*

84 Three varieties of Zn-rich trioctahedral smectites and one Mg-stevensite were synthesized
85 hydrothermally from gel precursors having adequate stoichiometry (Hamilton & Henderson,
86 1968). Preparation of a sauconite with ideal structural formula $[Na_{0.8}]^{inter}[Zn_{6.0}]^{octa}[Si_{7.2}$
87 $Al_{0.8}]^{tetra}O_{20}(OH)_4$ (hereafter referred to as Zn-sap), a Zn equivalent of hectorite with ideal
88 composition $[Na_{0.8}]^{inter}[Zn_{5.2}Li_{0.8}]^{octa}[Si_{8.0}]^{tetra}O_{20}(OH)_4$ (hereafter referred to as Zn-hect); a Zn
89 equivalent of stevensite with ideal structural formula $[Na_{0.8}]^{inter}[Zn_{5.6}\square_{0.4}]^{octa}[Si_{8.0}]^{tetra}O_{20}(OH)_4$
90 (hereafter referred to as Zn-stev), and stevensite with an ideal structural formula
91 $[Na_{0.8}]^{inter}[Mg_{5.6}\square_{0.4}]^{octa}[Si_{8.0}]^{tetra}O_{20}(OH)_4$ (hereafter referred to as Mg-Stev) was sought. All
92 structural formulae are derived from the stoichiometry of gel precursors. Such an ideal
93 sauconite composition leads however to the crystallization of a hemimorphite impurity
94 ($Zn_4Si_2O_7(OH)_4 \cdot H_2O$) and a lower Zn content is necessary to obtain pure sauconite (Higashi *et*
95 *al.*, 2002). The Na:Al:Si:Zn ratio of the initial gel was thus modified to 0.8:0.8:7.2:5.0 leading
96 to the following approximate structural formula:
97 $[Na_{0.84}]^{inter}[Zn_{5.24}Al_{0.38}\square_{0.38}]^{octa}[Si_{7.53}Al_{0.47}]^{tetra}O_{20}(OH)_4$. Synthesis of Zn-smectites was

98 performed in Teflon lined Parr reactor (45mL). Initial gels were treated hydrothermally under
99 autogenous pressure for 2 weeks at 170 °C for Zn-stev and Zn-hect, and for 3 days at 220 °C
100 for Zn-sap. Mg-stev synthesis was performed in an externally heated Morey-type pressure
101 vessel with an internal silver tubing (Robert *et al.*, 1993; Bergaoui *et al.*, 1995). Synthesis
102 conditions were a temperature of 300 °C, a water pressure of 500 bars, and a duration of 2
103 weeks. After synthesis, all samples were Na-saturated by contact with a 1 mol L⁻¹ aqueous
104 solution of NaCl. To ensure a complete exchange of interlayer cations, samples were shaken
105 mechanically in this NaCl solution for 24 h before separation of the solid fraction by
106 centrifugation. Excess NaCl was then removed by washing the solid three times with deionized
107 water (Siemens UltraClear, 18.2 MΩ cm⁻¹) and separation of the solid fraction by
108 centrifugation.

109 *Experimental Sample Characterization*

110 Water vapor sorption isotherms were determined volumetrically at 25 °C from sample powder
111 using a Belsorp-max instrument from BEL Japan. Lyophilized aliquots (~100 mg) were initially
112 outgassed at 150 °C for 24 h under a residual pressure of 10⁻⁵–10⁻⁴ Pa. In addition, N₂ BET
113 surface areas were determined on all Na-saturated samples with the same instrument.

114 Oriented slides were prepared for all samples by pipetting an aqueous clay slurry on glass
115 slides and drying it at room temperature. The amount of deposited material was weighed. An
116 aluminum slide was used for saucnite preparation to overcome peeling and curling issues. X-
117 ray diffraction (XRD) patterns were then recorded using a Bruker D8 diffractometer operated
118 at 40 kV and 40 mA and equipped with a MHG Messtechnik humidity controller coupled to an
119 Anton Paar CHC+ chamber. Intensities were measured for 6s per 0.04 °2θ step over the
120 2–50 °2θ Cu Kα angular range with a SolXE Si(Li) solid-state detector (Baltic Scientific
121 Instruments). Divergence slit, the two Soller, antiscatter, and resolution slits were 0.3°, 2.3°,
122 0.3°, and 0.1°, respectively. Samples were maintained at 23 °C in the CHC+ chamber during
123 data collection, whereas the desired relative humidity (RH) value was maintained by using a
124 constant flow of mixed dry/saturated air. RH was continuously monitored with a hygrometer
125 (uncertainty of ~2% RH) located close to the sample along the whole isotherm. Samples were
126 equilibrated at ~95% RH for 8h (Mg-stev) or 4h (Zn-hect, Zn-sap, and Zn-stev) before starting
127 data collection. Along the desorption isotherm, samples were equilibrated for 2 h at each
128 given RH value before XRD data collection, hydration stability being systematically checked by

129 recording again the low-angle reflection after collection of a complete XRD pattern. In
130 addition, all samples were exposed to ethylene glycol (EG) vapor (40 °C) overnight before XRD
131 data collection at 23 °C and room temperature. XRD data was also collected after a similar EG
132 solvation of samples heated to 350 °C for 1 h. Routine data processing, including
133 determination of basal reflection FWHM, was performed using the Eva® program from Bruker.
134 XRD data modeling was performed as described previously (Ferrage *et al.*, 2005a, 2005b, 2010;
135 Dazas *et al.*, 2015; Vinci *et al.*, 2020). Briefly, a main structure, periodic (that is with only one
136 layer type) if possible, was used to reproduce as much as possible of the data. Additional
137 contributions to the diffracted intensity were then introduced to account for the misfit. Up to
138 four interstratified structures, each with a different composition (relative proportion of the
139 different layer types), were necessary to reproduce some of the XRD patterns because of the
140 observed hydration heterogeneity. Interstratification of the different types of hydrated layers
141 was essentially random in all contributions to the diffracted intensity. Ordered
142 interstratification was used to reproduce low-angle reflections, however. In this case, the
143 Reichweite parameter was set to 1, and maximum possible degree of ordering was
144 considered, thus prohibiting the succession of two layers of the minor layer type (Drits &
145 Tchoubar, 1990; Sakharov & Lanson, 2013).

146

147 **Results and discussion**

148 *Powder X-ray diffraction*

149 Hydration modification of Zn-rich stevensite along the desorption isotherm induces a steady
150 decrease of the d -spacing corresponding to the first basal reflection from ~ 15.9 Å to ~ 10.1 Å
151 at 90% and 10% RH, respectively (Figs. 1A, S11). Except for the peak at 3.1-3.2 Å, which is
152 common to all usual hydration states (0W, 1W, 2W, and 3W), higher-order reflections are
153 weak and do not define a rational series of 00 l reflections (Fig. 1A), indicative of a major
154 hydration heterogeneity. By contrast, a low-angle reflection, that is likely related to the
155 regular alternation of two hydration states, is visible at 21-22 Å for XRD patterns collected
156 from 70 to 30% RH (arrows in Fig. 1A). Upon EG solvation, Zn-stev d_{001} increases to ~ 17.1 Å, as
157 expected for smectite (Fig. 1B), and positions of 002 and 005 reflections are about rational
158 with that of the 001, thus indicating little interstratification with non-swelling layers, if any. In

159 addition, the presence of a significant amount of talc-like layers Zn-stev would, after EG
160 solvation, induce a significant broadening of the first basal reflection compared to reflections
161 occurring at higher angle, inconsistent with the data (Fig. S12). Hydration behavior of Zn-sap
162 and Zn-hect (Figs. S13, S14) are consistent with those of their Mg equivalent having similar layer
163 charge (Fig. 1 in Ferrage *et al.*, 2010; Fig. 2 in Dazas *et al.*, 2013) and indicate slightly higher
164 hydration at low RH values. Position of smectite first basal reflection at 20% RH correspond
165 indeed to an apparent layer-to-layer distance of 10.2 Å for Zn-stev compared to 12.4 and
166 11.6 Å for Zn-sap and Zn-hect, respectively (Fig. 1B – 12.35 and 12.45 Å for Mg-sap and Mg-
167 hect, respectively).

168 XRD patterns of Mg-stev collected along the water vapor desorption isotherm differ
169 significantly from those of its Zn counterpart (Fig. 2A). Specifically, the first basal reflection is
170 systematically located between the positions expected for 1W and 0W smectite, thus
171 indicating a consistently low hydration state, possibly as the result of an incomplete
172 rehydration after drying. Rehydration of stevensite (both Zn- and Mg-stev) appears indeed to
173 be slow (up to several days or even weeks) after drying the sample. The position of this first
174 basal reflection steadily shifts towards higher angles with decreasing RH, whereas higher-
175 order reflections are systematically visible at 4.7-4.8 Å and 3.15-3.20 Å. In addition, a low-
176 angle reflection is visible, its position shifting from ~22.5 to ~17 Å when RH decreases from 95
177 to 45% (arrows in Fig. 2A). Similar to Zn-stev, Mg-stev d_{001} increases to ~17 Å upon EG
178 solvation, as expected for smectite (Fig. 2B). Positions of higher-order reflections (at ~9.8,
179 5.67, and 3.35 Å) indicate however the possible interstratification with non-expandable or
180 collapsed layers. By contrast, XRD patterns of Mg-sap and Mg-hect displays two series of
181 almost rational 00 l reflections after EG solvation, both corresponding to layer-to-layer
182 distances of ~16.9 Å (Fig. 2B).

183 When plotting the full width at half maximum intensity (FWHM) of the first basal
184 reflection as a function of its position (Fig. 3), one may note the significant broadening of Zn-
185 smectite basal reflections compared to their Mg equivalents, except for stevensite. This
186 increase in FWHM is most likely related to the lower crystallinity of Zn smectite in relation to
187 their lower synthesis temperature (170-220 °C compared to 300-400 °C for Mg-smectites). In
188 all cases, XRD peak breadth is positively correlated to specific surface area values (Table 1),
189 evidencing the major influence of crystallinity on both values. Compared to Mg-sap and Mg-

190 hect, crystallinity of Mg-stev is significantly degraded owing to the lower synthesis
191 temperature and duration (400 °C for 1 month for Mg-hect and Mg-sap compared to 300 °C
192 for 2 weeks for Mg-stev). In addition, FWHM is minimal for Mg-sap and Mg-hect for apparent
193 d_{001} values of ~ 15.5 and ~ 12.4 Å, that correspond to typical layer-to-layer distances of 2W and
194 1W smectites (Bradley *et al.*, 1937; Norrish, 1954a; Ferrage *et al.*, 2010; Dazas *et al.*, 2013).
195 These minimal FWHM values correspond to optimal hydration homogeneity with about 90%
196 of the layers or more having the same hydration state (Ferrage *et al.*, 2005b; Aristilde *et al.*,
197 2013). On this plot, FWHM values determined for Mg-hect are systematically higher than the
198 ones determined for Mg-sap and Mg-hect. This is possibly related to the lower temperature
199 used for the synthesis of the former sample (300 °C compared to 400 °C for Mg-sap and Mg-
200 hect). One may note however that FWHM values of Mg-stev are decreasing as its apparent
201 d_{001} value is decreasing to match the typical layer-to-layer distance of 0W Na-saturated
202 smectite (9.6 Å), as a possible indication of decreased hydration heterogeneity. Consistent
203 with Mg-sap and Mg-hect, the three Zn-smectites exhibit minimal values of FWHM for $d_{001} \approx$
204 15.5 Å (Fig. 3 – triangles). A second minimum for $d_{001} \approx 12.4$ Å is observed only for Zn-sap,
205 however, FWHM values steadily decreasing for both Zn-hect and Zn-stev for d_{001} values lower
206 than ~ 14.5 Å. For Zn-stev, FWHM values actually come to a minimum for $d_{002} \approx 11.0$ -11.3 Å
207 (dotted-dashed ellipse in Fig. 3), that possibly corresponds to the second-order of the low-
208 angle maximum. Similar low FWHM values are observed when Zn-stev is fully dehydrated (d_{001}
209 ≤ 10.0 Å).

210 *Water vapor desorption isotherms*

211 The comparison of H₂O vapor desorption isotherms obtained for stevensite and for their
212 hectorite/saponite counterparts shows that, for a given chemistry (i.e. for Zn- and Mg-
213 smectites), H₂O contents are similar for both hectorite and saponite, whereas H₂O content is
214 decreased by ~ 2.0 -2.5 mmol g⁻¹ in stevensite (Fig. 4). For example, at 30% RH, both Mg- and
215 Zn-stev accommodate ~ 2.0 mmol H₂O per g of dry clay whereas the saponite and hectorite
216 equivalent host ~ 5 and ~ 4 mmol H₂O per g of dry clay (Mg- and Zn-smectites, respectively).
217 The different H₂O contents determined for Zn- and Mg-sap/hect essentially result from the
218 difference in molecular weights for the two chemical compositions.

219 In addition, the transition between the two plateaus corresponding to 1W and 2W
220 hydration states (4-7 and 10-14 mmol H₂O per g of dry clay, respectively, for Mg-sap/hect –

221 gray areas in Fig. 4) differs significantly from hectorite and saponite on the one hand and
222 stevensite on the other hand. For Mg-smectites, the transition spreads from ~60 to ~40% RH
223 for both saponite and hectorite whereas no transition is visible for stevensite, consistent with
224 the almost constant position of the first basal reflection at ~10.2 Å. For Zn-smectites, the
225 transition appears smoother than for Mg-smectites, possibly as the result of the lower
226 crystallinity and synthesis temperature (Table 1 – Michot *et al.*, 2005). Compared to Mg-
227 smectites, this 2W-to-1W transition also appears shifted to lower RH values and spreads from
228 ~50% to ~35% RH. In contrast to Mg-smectites, the transition is visible for all three Zn smectite
229 varieties, including Zn-stev, although Zn-stev seems to exhibit no stable 1W hydration state.

230 *X-ray diffraction profile modeling*

231 XRD profile modeling allows gaining additional insights into the hydration behavior of
232 stevensite relative to other trioctahedral smectite varieties (saponite and hectorite). The
233 lower temperatures used to synthesize stevensite, compared to saponite/hectorite, strongly
234 degrade the crystallinity of the synthetic smectite product. As a consequence, the intensity
235 and resolution of high-angle reflections are lowered thus hampering the determination of
236 interlayer H₂O structure. The relative proportions of the different smectite hydration states
237 coexisting at a given relative humidity can be deduced however from the modeling of the low-
238 angle region (2-30 °2θ Cu Kα). Fits to the data are provided as supplementary information
239 (Figs SI1, SI3-SI4) together with the composition of the different contributions to the
240 calculated diffraction patterns (Tables SI1-SI3).

241 Compared to Mg-sap/hect (Ferrage *et al.*, 2010; Dazas *et al.*, 2015; Vinci *et al.*, 2020),
242 hydration appears much more heterogeneous in Zn-smectites (Fig. 5; Tables SI1-SI3). The
243 proportion of a given hydration state (0W, 1W, 2W, or 3W) never exceeds 75%, except for
244 dehydrated layers in Zn-stev for RH conditions below 25% RH (Fig. 5). This increased
245 heterogeneity is possibly linked to an increased chemical heterogeneity in relation to lower
246 synthesis temperature. This effect is likely enhanced by the decrease in crystallinity that
247 smoothens the transition between defined hydration states (Michot *et al.*, 2005). In apparent
248 contradiction with H₂O vapor desorption isotherms, prevalence of 1W layers over 2W layers
249 initiates at higher RH conditions for Zn-smectites (60-50% and 70-60% RH for Zn-sap and Zn-
250 hect, respectively), compared to their Mg equivalent. Zn-stev dehydration occurs even at

251 higher humidity conditions as the proportions of 2W Zn-stev layers is null at 50% RH and
252 below, whereas Zn-sap and Zn-hect still contain ~35 and 25%, respectively, of 2W layers at
253 50% RH. Similarly, 0W layers prevail in Zn-stev from 60% RH down to 0% RH, whereas these
254 layers prevail only at 10% RH in Zn-hect (Fig. 5). It is noteworthy that 1W layers never prevail
255 in Zn-stev, whatever the RH conditions, consistent with the absence of a FWHM minimum
256 corresponding to a layer-to-layer distance typical for this hydration state (Fig. 3). Although 1W
257 layers prevail in Zn-hect from 65% to 15%RH, the relative proportions of these layers never
258 exceeds ~60%, the high hydration heterogeneity being in this case responsible for the absence
259 of a FWHM minimum corresponding to a layer-to-layer distance typical for 1W layers (Fig. 3).

260 Finally, fitting the low-angle maximum of both Zn-stev and Mg-stev required a
261 contribution from a regular 1:1 interstratification of 0W and 1W layers (Fig. SI5, Table SI1).
262 This ordered interstratification allowed fitting the low-angle reflection at 20-22 Å, consistent
263 with previous reports and hypotheses (Brindley, 1955; Faust *et al.*, 1959; Shimoda, 1971),
264 although interstratification implied 0W and 1W layers rather than 0W and 2W, as previously
265 hypothesized. The presence, and major contribution, of this regular interstratification (mixed-
266 layer #4 in Table SI1) also accounts for the minimum FWHM observed in the XRD patterns of
267 Zn-stev in which the position of the first basal reflection is 11.0-11.3 Å (Fig. 3).

268 *Swelling ability and stevensite identification*

269 To differentiate stevensite from other trioctahedral smectites (saponite/hectorite) Christidis
270 and Koustopoulou (2013) proposed to saturate smectites with EG after heating to 500 °C.
271 Upon this dual treatment, saponite and hectorite expand whereas stevensite layers remain
272 collapsed. The criterion proposed by these authors appear valid for Mg-hect and Mg-stev, the
273 former re-expanding almost completely to ~17 Å after heating to 350 °C and EG solvation
274 whereas Mg-stev remains essentially collapsed to ~9.6 Å (Fig. 6A). By contrast, both Zn-stev
275 and Zn-hect do not re-expand after the same treatment whereas Zn-sap swelling ability is
276 essentially unaffected (Fig. 6B). The origin of the contrasting swelling behavior observed for
277 hectorite depending on its octahedral composition remains unexplained but pleads for
278 additional investigation to assess the validity of identification criterion proposed by Christidis
279 and Koustopoulou (2013). In particular, it is necessary to assess the influence i) of crystallinity
280 on smectite hydration behavior, ii) of the octahedral composition on the hectorite ability to
281 re-expand upon heating and EG solvation, and iii) of the possible layer heterogeneity resulting

282 from the presence of stevensite- and talc-like domains/layers in synthetic smectites (Christidis
283 *et al.*, 2018).

284

285 **Conclusion**

286 For a given layer charge ($\sim 0.8 e^-$ per $O_{20}(OH)_4$ in the present study) and chemical composition,
287 the H_2O content is lower (by ~ 2.0 mmol H_2O per g of dry clay) in stevensite compared to its
288 hectorite and saponite equivalents. As a result of this lower H_2O content, the transition from
289 prevailing 2W to prevailing 1W hydration states occurs at slightly higher RH values for Zn-stev
290 compared to Zn-sap and Zn-hect. Hydration behavior of Zn-sap and Zn-hect is similar to that
291 of their Mg counterparts. In addition, 1W layers never prevail in Zn-stev, whatever the H_2O
292 activity, the position of its first basal reflection shifting steadily from an apparent d_{001} of
293 15.5 \AA , consistent with the prevalence of 2W layers, to $\sim 9.6 \text{ \AA}$, consistent with Zn-stev
294 complete dehydration. Dehydrated layers prevail in Zn-stev from 60% RH down to 0% RH.
295 Finally, the low-angle reflection commonly observed for stevensite under air-dried conditions
296 is due to the presence of the regular interstratification of 0W and 1W layers.

297 With respect to stevensite identification from X-ray diffraction of heated and EG-
298 solvated samples (Christidis & Koutsopoulou, 2013), the chemical composition of the
299 octahedral sheet (Zn or Mg in the present study) appears to strongly modify hectorite swelling
300 behavior, thus challenging the method. Further research is needed to decipher the origin of
301 this effect and to propose a more general identification method.

302

303 **Acknowledgments**

304 DV thanks U. Bari from granting her a Ph.D. fellowship. The CNRS interdisciplinary défi Needs,
305 through its “MiPor” program, is thanked for the financial support to the present study. ISTerre
306 is part of Labex OSUG@2020 (ANR10 LABX56).

307

308

309 **References**

- 310 Aristilde L., Lanson B. & Charlet L. (2013) Interstratification patterns from the pH-dependent
311 intercalation of a tetracycline antibiotic within montmorillonite layers. *Langmuir*, **29**,
312 4492-4501.
- 313 Bentz J.L. & Peterson R.C. (2020) The formation of clay minerals in the mudflats of Bolivian
314 salars. *Clays and Clay Minerals*, **68**, 115-134.
- 315 Bergaoui L., Lambert J.-F., Franck R., Suquet H. & Robert J.-L. (1995) Al-pillared saponites. Part
316 3.—effect of parent clay layer charge on the intercalation–pillaring mechanism and
317 structural properties. *Journal of the Chemical Society, Faraday Transactions*, **91**, 2229-
318 2239.
- 319 Bradley W.F., Grim R.E. & Clark G.F. (1937) A study of the behavior of montmorillonite upon
320 wetting. *Zeitschrift für Kristallographie*, **97**, 216-222.
- 321 Brindley G.W. (1955) Stevensite, a montmorillonite-type mineral showing mixed-layer
322 characteristics. *American Mineralogist*, **40**, 239-247.
- 323 Brindley G.W. (1980) Order-disorder in clay mineral structures. Pp. 125-195. In G.W. Brindley,
324 and G. Brown, Eds. *Crystal structures of clay minerals and their X-ray identification*,
325 Mineralogical Society, London.
- 326 Christidis G.E. & Koutsopoulou E. (2013) A simple approach to the identification of
327 trioctahedral smectites by X-ray diffraction. *Clay Minerals*, **48**, 687-696.
- 328 Christidis G.E., Aldana C., Chryssikos G.D., Gionis V., Kalo H., Stöter M., Breu J. & Robert J.-L.
329 (2018) The nature of laponite: Pure hectorite or a mixture of different trioctahedral
330 phases? *Minerals*, **8**, 314.
- 331 Dazas B., Lanson B., Breu J., Robert J.L., Pelletier M. & Ferrage E. (2013) Smectite fluorination
332 and its impact on interlayer water content and structure: A way to fine tune the
333 hydrophilicity of clay surfaces? *Microporous and Mesoporous Materials*, **181**, 233-247.
- 334 Dazas B., Lanson B., Delville A., Robert J.-L., Komarneni S., Michot L.J. & Ferrage E. (2015)
335 Influence of tetrahedral layer charge on the organization of interlayer water and ions
336 in synthetic Na-saturated smectites. *The Journal of Physical Chemistry C*, **119**, 4158-
337 4172.

338 de Oliveira Nardi Leite C., de Assis Silva C.M. & de Ros L.F. (2020) Depositional and diagenetic
339 processes in the pre-salt rift section of a Santos basin area, SE Brazil. *Journal of*
340 *Sedimentary Research*, **90**, 584-608.

341 Drits V.A. & Tchoubar C. (1990) *X-ray diffraction by disordered lamellar structures: Theory*
342 *and applications to microdivided silicates and carbons*. Pp. 371. Springer-Verlag,
343 Berlin.

344 Eberl D.D., Jones B.F. & Khoury H.N. (1982) Mixed-layer kerolite/stevensite from the
345 Amargosa desert, Nevada. *Clays & Clay Minerals*, **30**, 321-326.

346 Faust G.T., Hathaway J.C. & Millot G. (1959) A restudy of stevensite and allied minerals.
347 *American Mineralogist*, **44**, 342-370.

348 Ferrage E., Lanson B., Malikova N., Plancon A., Sakharov B.A. & Drits V.A. (2005a) New insights
349 on the distribution of interlayer water in bi-hydrated smectite from X-ray diffraction
350 profile modeling of 00l reflections. *Chemistry of Materials*, **17**, 3499-3512.

351 Ferrage E., Lanson B., Sakharov B.A. & Drits V.A. (2005b) Investigation of smectite hydration
352 properties by modeling experimental X-ray diffraction patterns: Part I.
353 Montmorillonite hydration properties. *American Mineralogist*, **90**, 1358-1374.

354 Ferrage E., Lanson B., Michot L.J. & Robert J.L. (2010) Hydration properties and interlayer
355 organization of water and ions in synthetic Na-smectite with tetrahedral layer charge.
356 Part 1. Results from X-ray diffraction profile modeling. *The Journal of Physical*
357 *Chemistry C*, **114**, 4515-4526.

358 Ferrage E., Sakharov B.A., Michot L.J., Delville A., Bauer A., Lanson B., Grangeon S., Frapper G.,
359 Jimenez-Ruiz M. & Cuello G.J. (2011) Hydration properties and interlayer organization
360 of water and ions in synthetic Na-smectite with tetrahedral layer charge. Part 2.
361 Towards a precise coupling between molecular simulations and diffraction data. *The*
362 *Journal of Physical Chemistry C*, **115**, 1867-1881.

363 Hamilton D.L. & Henderson C.M.B. (1968) The preparation of silicate compositions by a gelling
364 method. *Mineralogical Magazine*, **36**, 832-838.

365 Higashi S., Miki K. & Komarneni S. (2002) Hydrothermal synthesis of Zn-smectites. *Clays and*
366 *Clay Minerals*, **50**, 299-305.

367 Jones B.F. (1986) Clay mineral diagenesis in lacustrine environments. Pp. 291-300. In F.A.
368 Mumpton, Ed. *Studies in diagenesis*.

369 Khoury H.N., Eberl D.D. & Jones B.F. (1982) Origin of magnesium clays from the Amargosa
370 desert, Nevada. *Clays & Clay Minerals*, **30**, 327-336.

371 Laird D.A., Barak P., Nater E.A. & Dowdy R.H. (1991) Chemistry of smectitic and illitic phases
372 in interstratified soil smectite. *Soil Science Society of America Journal*, **55**, 1499-1504.

373 Malikova N., Cadene A., Marry V., Dubois E., Turq P., Zanotti J.M. & Longeville S. (2005)
374 Diffusion of water in clays - microscopic simulation and neutron scattering. *Chemical*
375 *Physics*, **317**, 226-235.

376 Malikova N., Cadene A., Dubois E., Marry V., Durand Vidal S., Turq P., Breu J., Longeville S. &
377 Zanotti J.M. (2007) Water diffusion in a synthetic hectorite clay studied by quasi-elastic
378 neutron scattering. *The Journal of Physical Chemistry C*, **111**, 17603-17611.

379 Michot L.J., Bihannic I., Pelletier M., Rinnert E. & Robert J.L. (2005) Hydration and swelling of
380 synthetic Na-saponites: Influence of layer charge. *American Mineralogist*, **90**, 166-172.

381 Michot L.J., Delville A., Humbert B., Plazanet M. & Levitz P. (2007) Diffusion of water in a
382 synthetic clay with tetrahedral charges by combined neutron time-of-flight
383 measurements and molecular dynamics simulations. *The Journal of Physical Chemistry*
384 *C*, **111**, 9818-9831.

385 Michot L.J., Ferrage E., Jiménez-Ruiz M., Boehm M. & Delville A. (2012) Anisotropic features
386 of water and ion dynamics in synthetic Na- and Ca-smectites with tetrahedral layer
387 charge. A combined quasi-elastic neutron-scattering and molecular dynamics
388 simulations study. *The Journal of Physical Chemistry C*, **116**, 16619-16633.

389 Mooney R.W., Keenan A.G. & Wood L.A. (1952) Adsorption of water by montmorillonite. II.
390 Effect of exchangeable ions and lattice swelling as measured by X-ray diffraction.
391 *Journal of the American Chemical Society*, **74**, 1371-1374.

392 Nagelschmidt G. (1936) On the lattice shrinkage and structure of montmorillonite. *Zeitschrift*
393 *für Kristallographie*, **93**, 481-487.

394 Norrish K. (1954a) Manner of swelling of montmorillonite. *Nature*, **173**, 256-257.

395 -. (1954b) The swelling of montmorillonite. *Discussions of the Faraday Society*, **18**, 120-133.

396 Rinnert E., Carteret C., Humbert B., Fragneto Cusani G., Ramsay J.D.F., Delville A., Robert J.L.,
397 Bihannic I., Pelletier M. & Michot L.J. (2005) Hydration of a synthetic clay with
398 tetrahedral charges: A multidisciplinary experimental and numerical study. *The Journal*
399 *of Physical Chemistry B*, **109**, 23745-23759.

400 Robert J.L., Beny J.M., Della Ventura G. & Hardy M. (1993) Fluorine in micas: Crystal-chemical
401 control of the OH-F distribution between trioctahedral and dioctahedral sites.
402 *European Journal of Mineralogy*, **5**, 7-18.

403 Sakharov B.A. & Lanson B. (2013) X-ray identification of mixed-layer structures. Modelling of
404 diffraction effects. Pp. 51-135. In F. Bergaya, and G. Lagaly, Eds. *Handbook of clay*
405 *science, Part B. Techniques and applications*, Elsevier, Amsterdam.

406 Shimoda S. (1971) Mineralogical studies of a species of stevensite from the Obori mine,
407 Yamagata prefecture, Japan. *Clay Minerals*, **9**, 185-192.

408 Thiry M., Milnes A. & Ben Brahim M. (2014) Pleistocene cold climate groundwater
409 silicification, Jbel Ghassoul region, Missouri basin, Morocco. *Journal of the Geological*
410 *Society*, **172**, 125-137.

411 Vinci D., Dazas B., Ferrage E., Lanson M., Magnin V., Findling N. & Lanson B. (2020) Influence
412 of layer charge on hydration properties of synthetic octahedrally-charged Na-
413 saturated trioctahedral swelling phyllosilicates. *Applied Clay Science*, **184**, 105404.

414

415 **Tables**

416 **Table 1.** Specific surface areas determined for Zn- and Mg-smectites with the BET method.

| Sample | Specific surface area (m ² /g) |
|---------|--|
| Mg-hect | 11.1 |
| Mg-sap | 50.1 |
| Mg-stev | 179.9 |
| Zn-hect | 146.9 |
| Zn-sap | 96.7 |
| Zn-stev | 100.7 |

417

418 **Figure captions**

419 **Fig. 1.** (A) X-ray diffraction patterns of Zn-stev along the H₂O vapor desorption isotherm. (B)
420 X-ray diffraction patterns of Zn-sap, Zn-hect, and Zn-stev collected at 20% RH (black lines),
421 70% RH (blue lines), and upon EG solvation (red lines). Dotted lines in (A) indicate the typical
422 positions of the first basal reflection for different smectite hydration states, arrows indicating
423 the position of low-angle reflection. Hal. Indicates the presence of halite. The vertical gray bar
424 indicates a modified scale factor for the high-angle region compared to the 2-15 °2θ range.

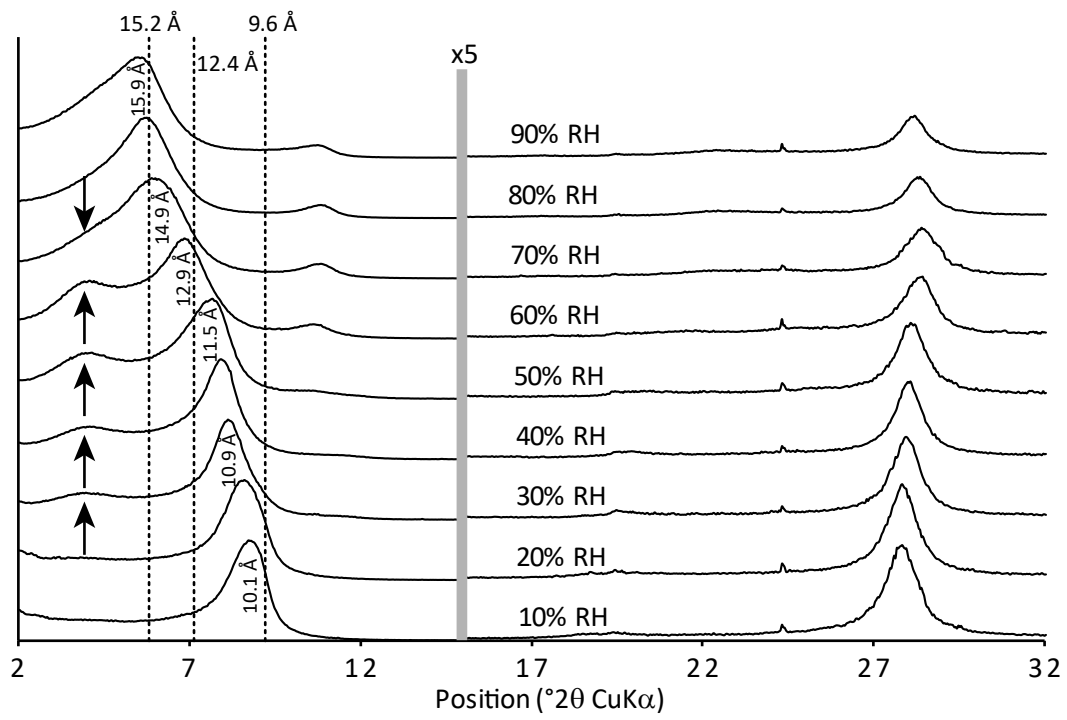
425 **Fig. 2.** (A) X-ray diffraction patterns of Mg-stev along the H₂O vapor desorption isotherm. (B)
426 X-ray diffraction patterns of Mg-sap, Mg-hect, and Mg-stev collected at 20% RH (black lines),
427 70% RH (blue lines), and upon EG solvation (red lines). Dotted lines in (A) indicate the typical
428 positions of the first basal reflection for different smectite hydration states, arrows indicating
429 the position of low-angle reflection. Hal. Indicates the presence of halite. The vertical gray bar
430 indicates a modified scale factor for the high-angle region compared to the 2-15 °2θ range s.

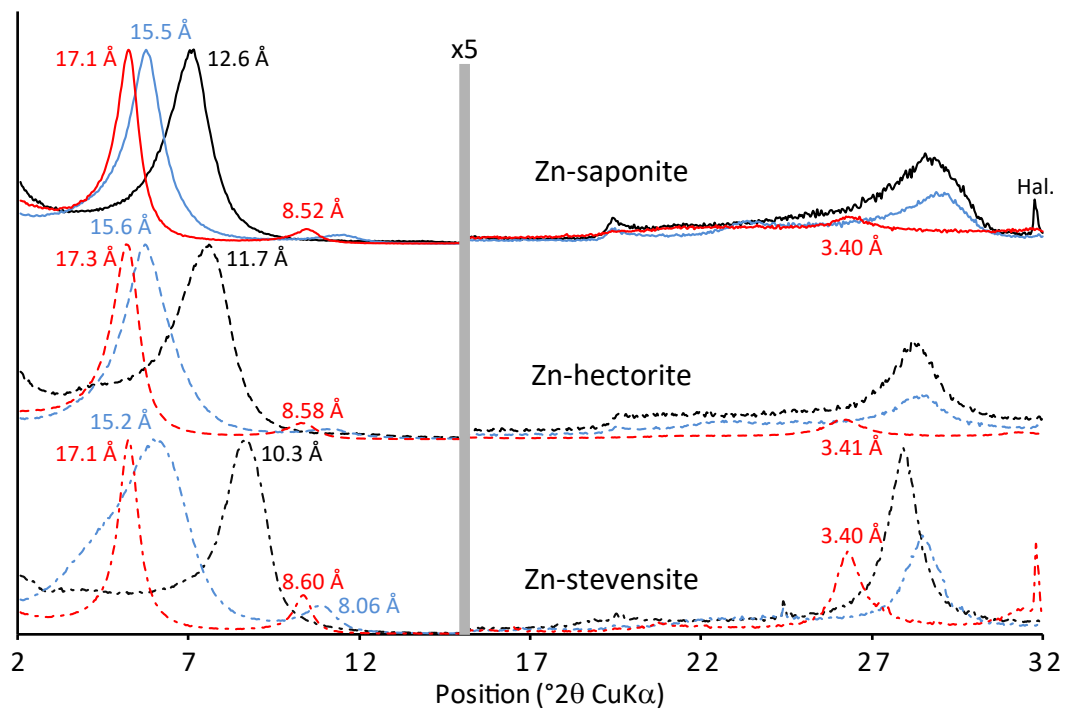
431 **Fig. 3.** Evolution of the full-width at half-maximum intensity (FWHM) of the first basal
432 reflection as a function of its position for Zn- and Mg-smectites (triangles and circles,
433 respectively). Data for Mg-smectites from Ferrage *et al.* (2010), Dazas *et al.* (2013), and Vinci
434 *et al.* (2020). The dashed ellipses highlight minimum FWHM values corresponding to
435 essentially homogeneous 1W and 2W hydration states. Position of the first basal reflection
436 essentially decreases with decreasing RH conditions during data collection from an initial
437 “wet” state at 90-95% RH depending on the sample..

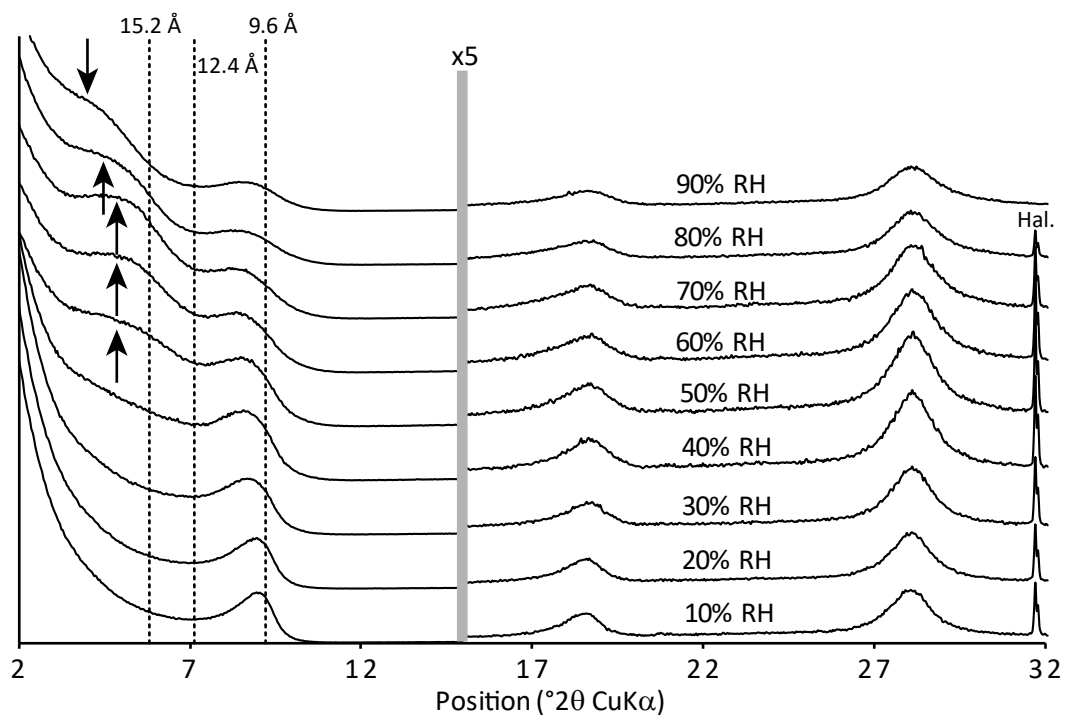
438 **Fig. 4.** Water content as a function of relative humidity along the water vapor desorption
439 isotherms. Dotted and solid lines represent Mg- and Zn-smectites, respectively. Mg-sap and
440 Mg-hect data from (Ferrage *et al.*, 2010) and (Dazas *et al.*, 2013), respectively. Gray areas
441 indicate the 1W and 2W plateaus occurring for Mg-sap/hect.

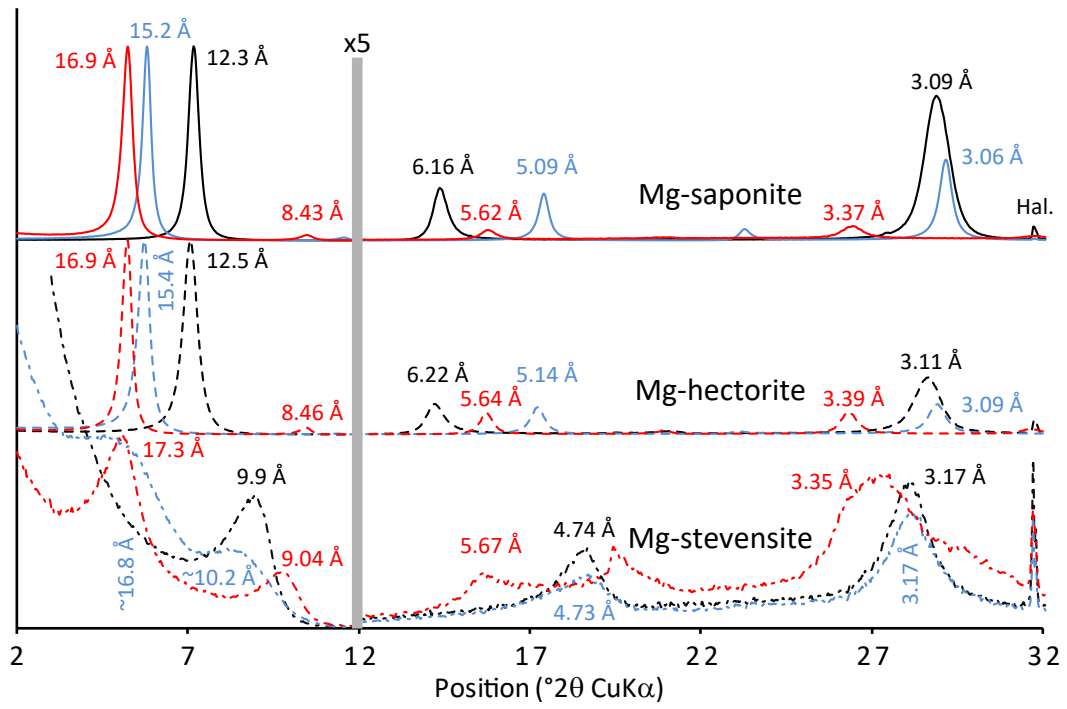
442 **Fig. 5.** Evolution of the relative proportions of the different layer types (summing up all
443 contributions to the diffracted intensity) along H₂O vapor desorption isotherms for Zn-stev,
444 Zn-hect, and Zn-sap.

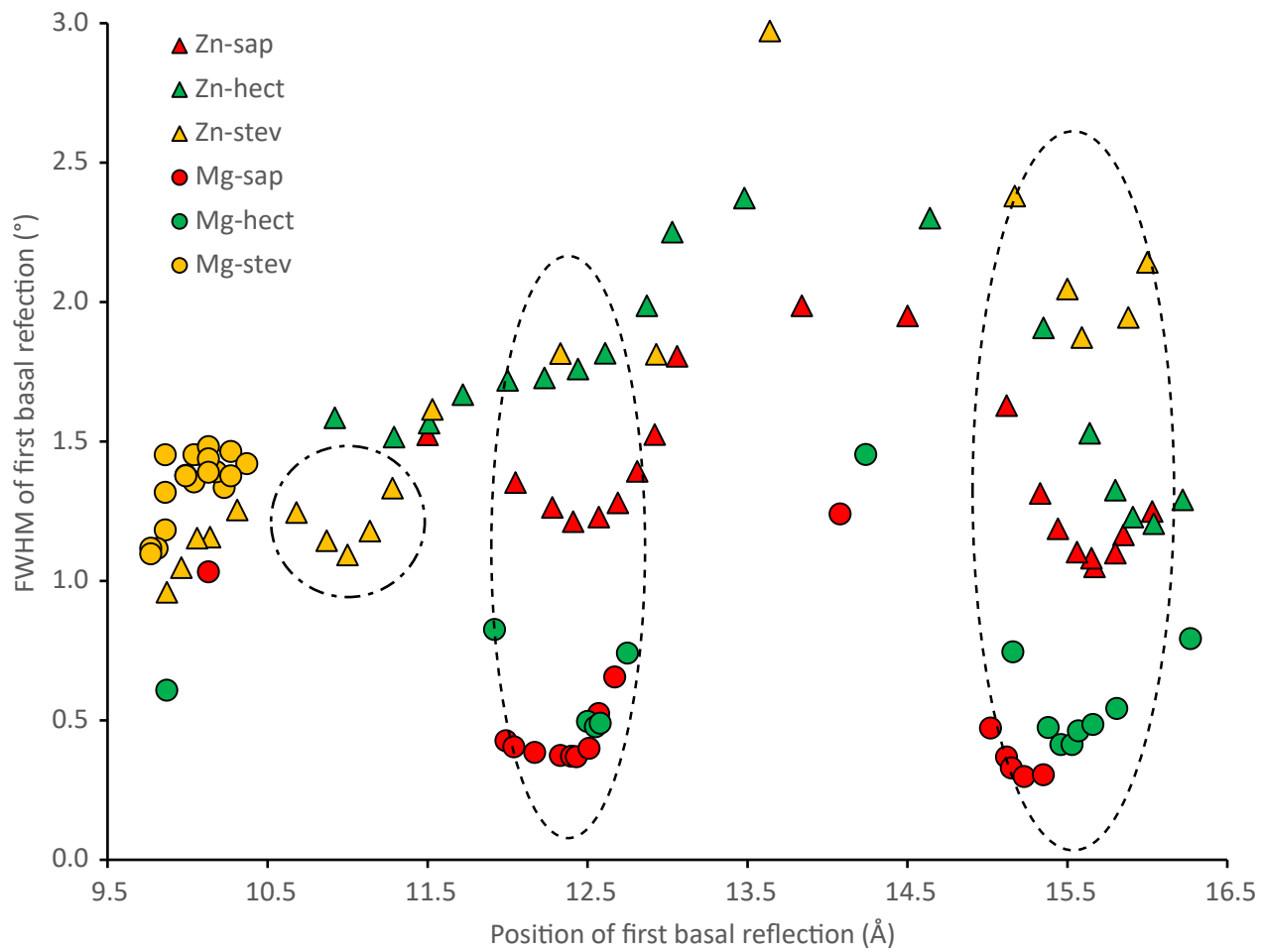
445 **Fig. 6.** Comparison of X-ray diffraction patterns obtained after EG solvation (red) and heating
446 to 350 °C followed by EG solvation (black). (A) Mg-smectites: Mg-hect (dashed lines), and Mg-
447 stev (dotted-dashed lines). (B) Zn-smectite: Zn-sap (solid lines), Zn-hect (dashed lines), and Zn-
448 stev (dotted-dashed lines). The vertical gray bar indicates a modified scale factor for the high-
449 angle region compared to the 2-12 °2θ range.



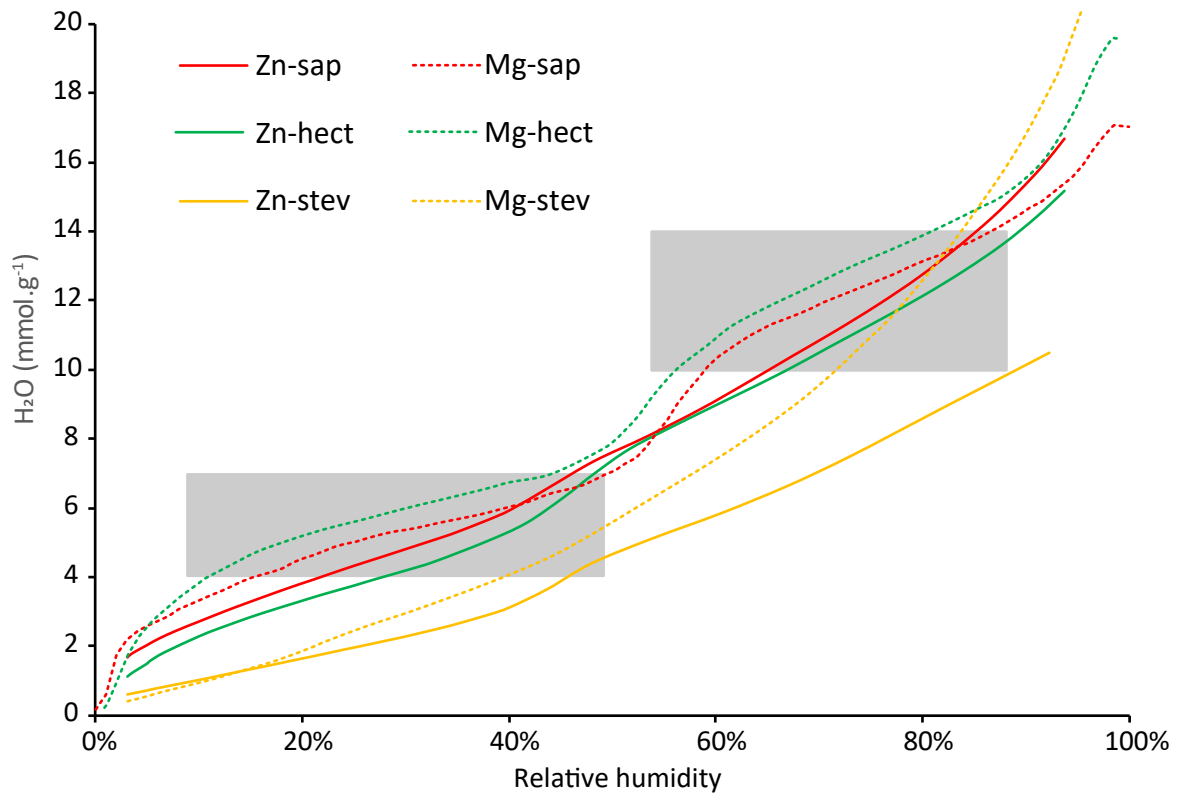


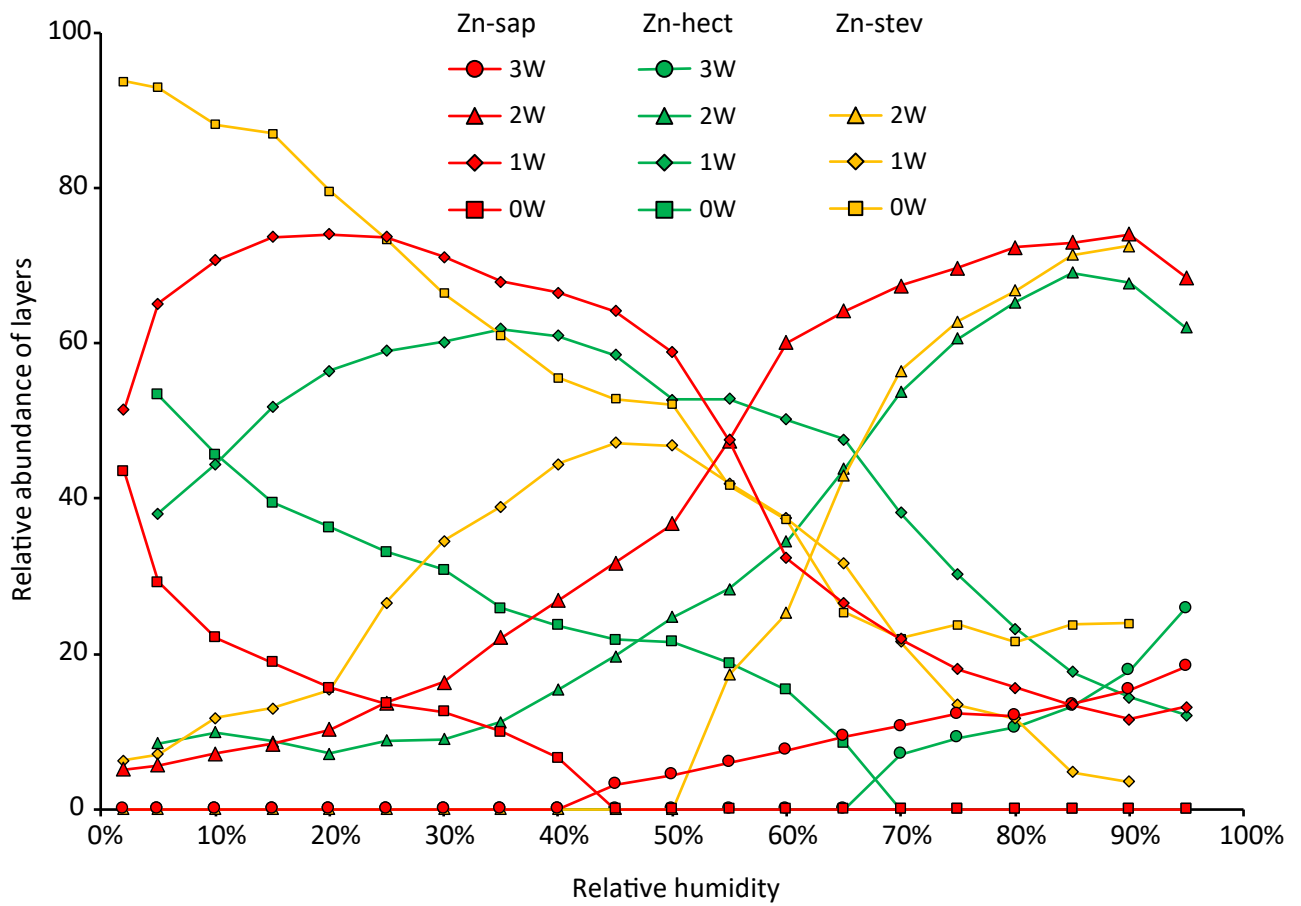


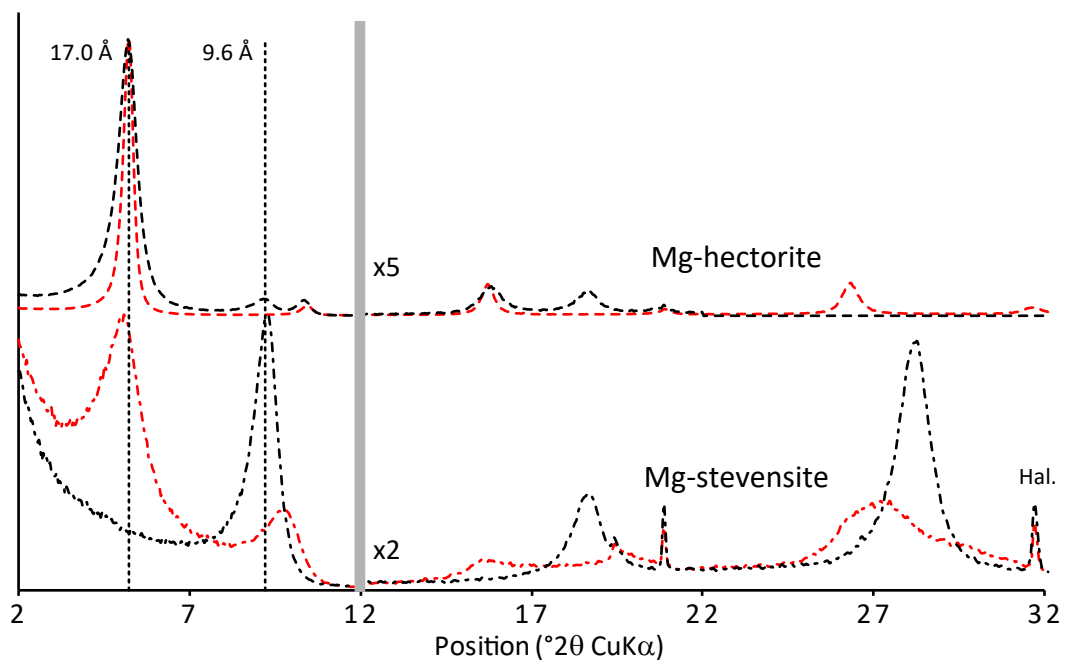


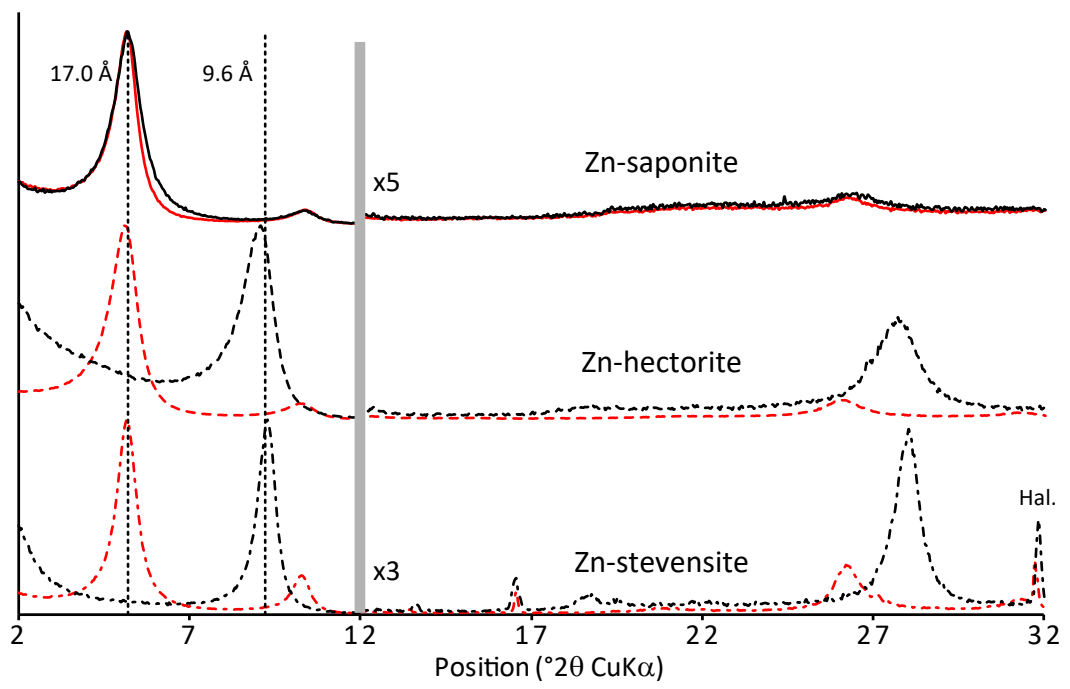


Please insert as a 2 column figure









Hydration of Na-saturated Synthetic Stevensite, a Peculiar Trioctahedral Smectite

Doriana Vinci^{1,2}, Bruno Lanson^{1,*}, Martine Lanson¹, Valérie Magnin¹, Nathaniel Findling¹

*Univ. Grenoble Alpes, Univ. Savoie Mont Blanc, CNRS, IRD, Univ. Gustave Eiffel, ISTerre, F-38000
Grenoble, France*

Dipartimento Scienze Terra & Geoambientali, Univ. Bari Aldo Moro, Bari, Italy

Running title: Hydration of Na-saturated Synthetic Stevensite

*. Corresponding author: bruno.lanson@univ-grenoble-alpes.fr

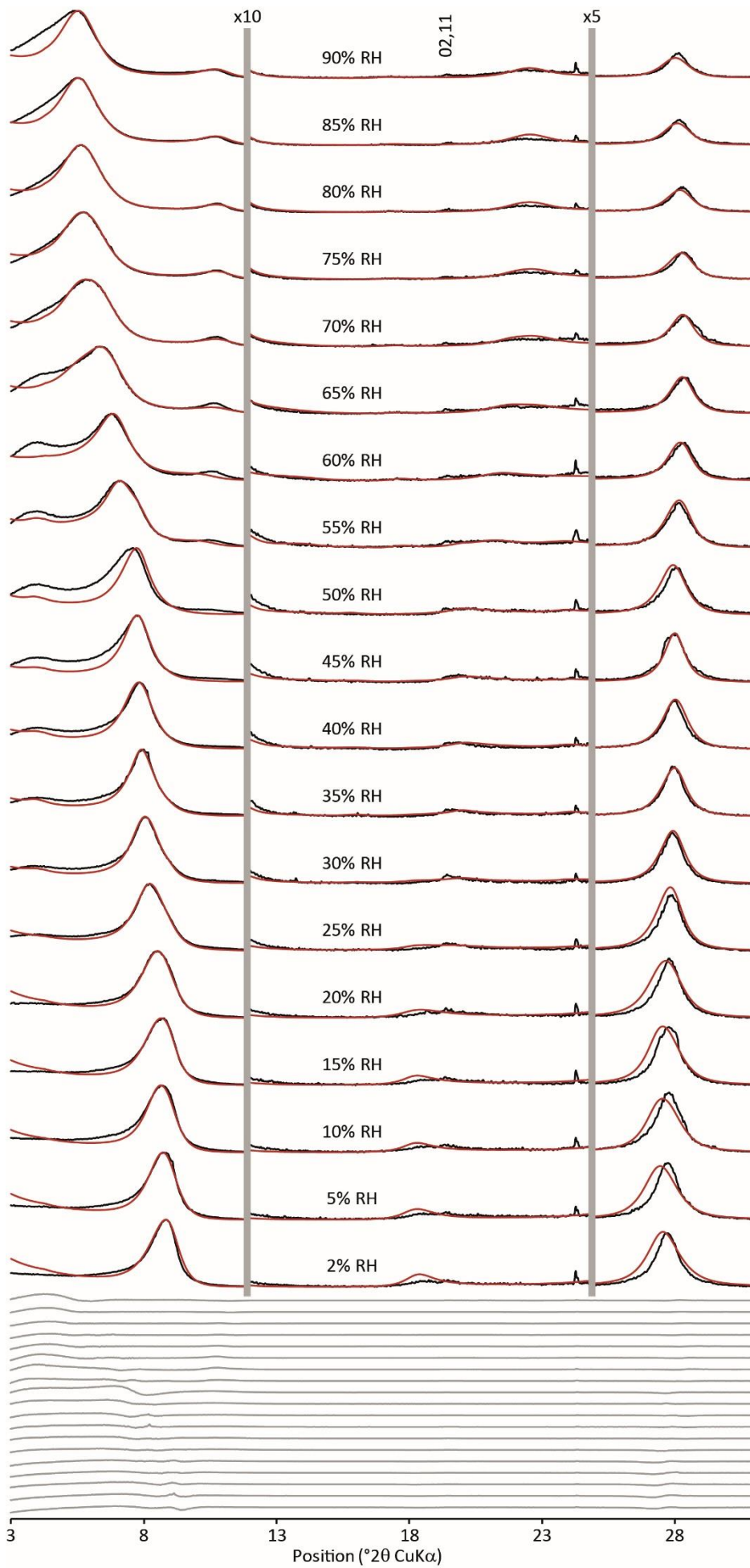


Fig. S11. Comparison between experimental and calculated XRD patterns along the H₂O vapor desorption isotherm for Zn-stev. Experimental and calculated XRD patterns are shown as solid red and black lines, respectively. Difference plots are shown at the bottom of the figure as gray lines. The vertical gray bar indicates a modified scale factor for the angle region higher to 12° 2θ compared to the 3-12 °2θ angular range. Diffraction lines from halite (NaCl) impurity are indicated as Hal.

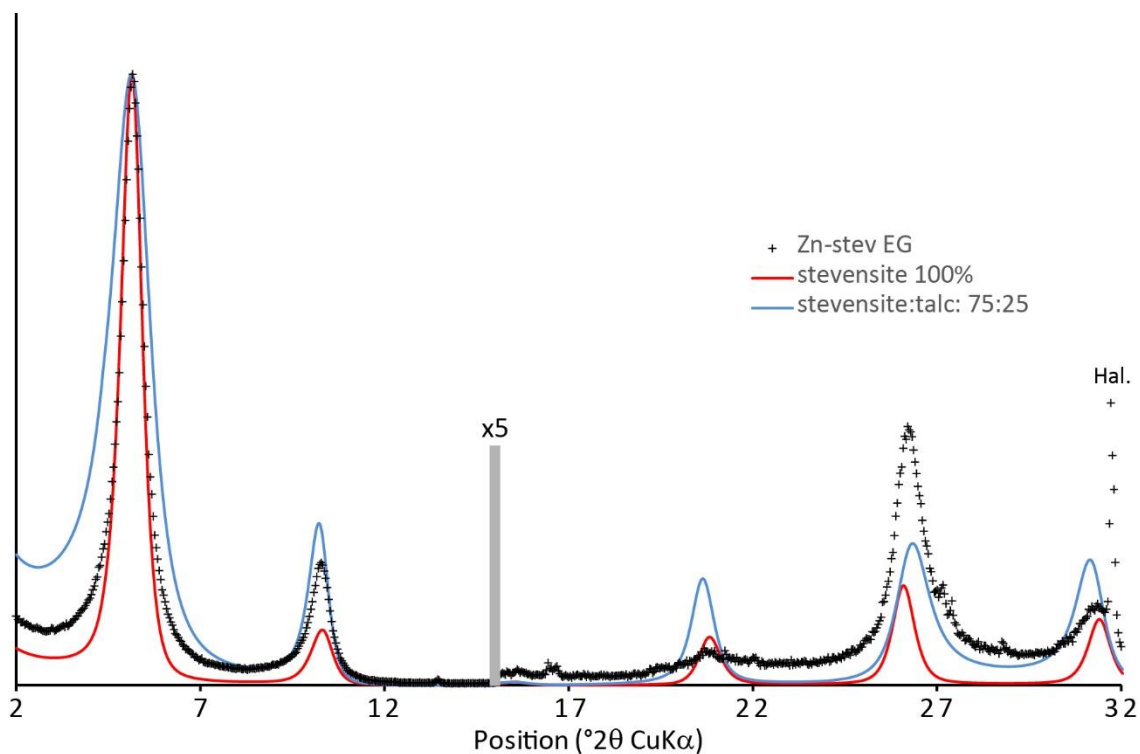


Fig. S12. Comparison between experimental and calculated XRD patterns for Zn-stev after EG solvation. Experimental data are shown as crosses. Solid red line and blue dashed line correspond to Zn-stev models containing 0 and 25% talc-like layers randomly interstratified with swelling layers. The latter value corresponds to the content of dehydrated (0W) layers in Zn-stev equilibrated at 90% RH (Table S11). Interlayer model for EG-solvated stevensite layers was not refined from that reported by Moore and Reynolds (1997). The vertical gray bar indicates a modified scale factor for the angle region higher to 15° 2θ compared to the 2-15° 2θ angular range. Diffraction line from halite (NaCl) impurity is indicated as Hal.

Reference cited

Moore D.M. & Reynolds R.C., Jr. (1997) *X-ray diffraction and the identification and analysis of clay minerals*. Pp. 378. Oxford University Press, Oxford.

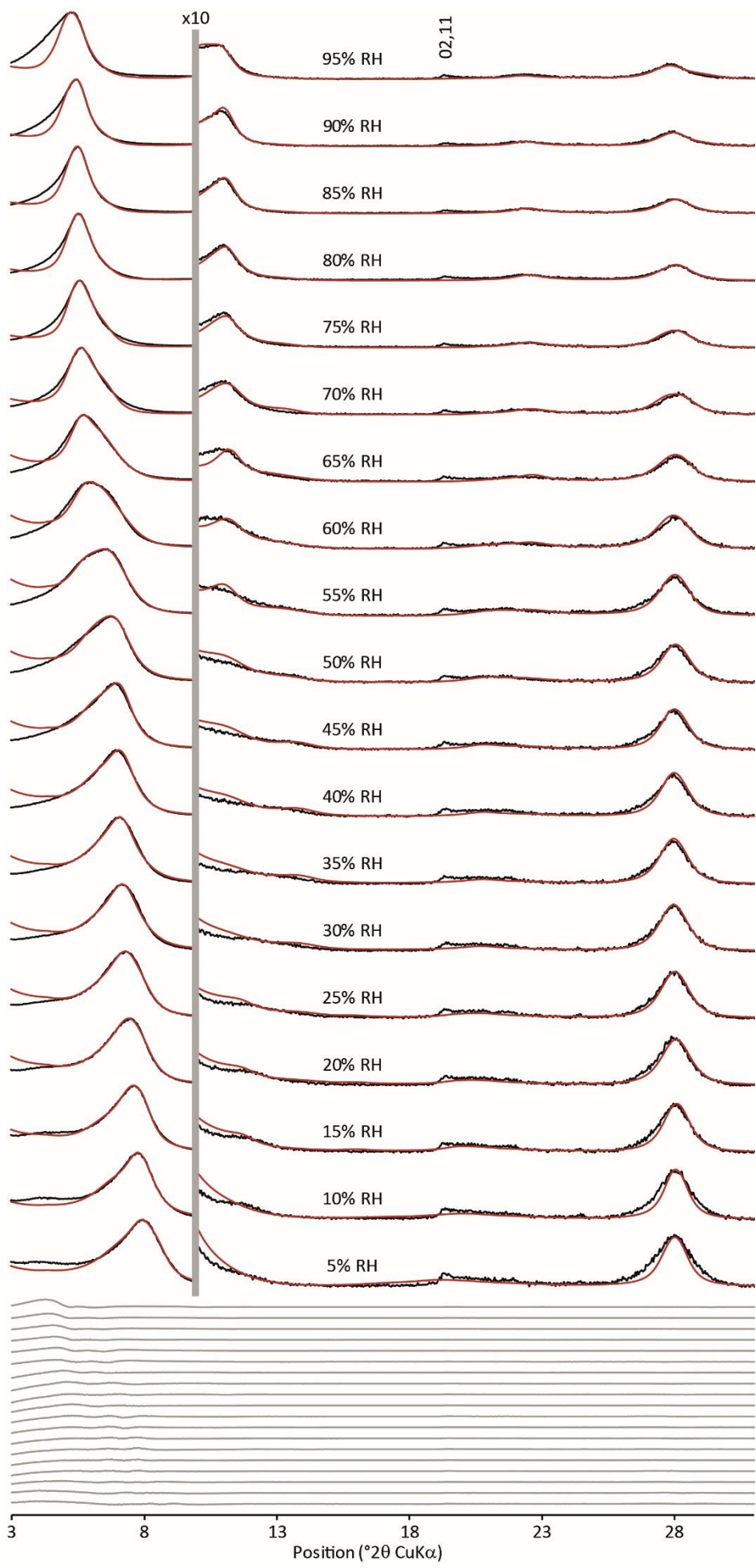


Fig. S13. Comparison between experimental and calculated XRD patterns along the H₂O vapor desorption isotherm for Zn-hect. Experimental and calculated XRD patterns are shown as solid red and black lines, respectively. Difference plots are shown at the bottom of the figure as gray lines. The vertical gray bar indicates a modified scale factor for the angle region higher to 10° 2θ compared to the 3-10 °2θ angular range.

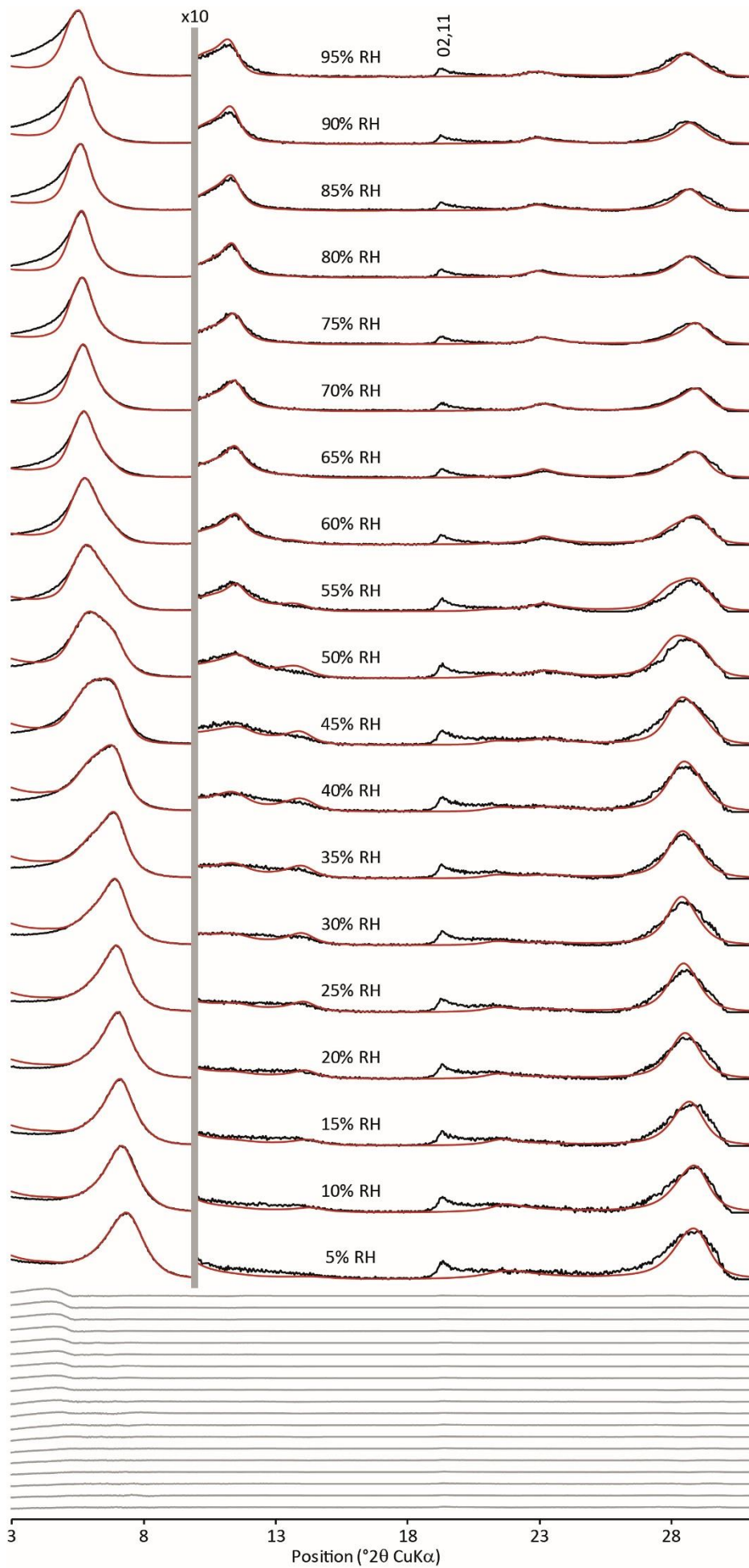


Fig. S14. Comparison between experimental and calculated XRD patterns along the H₂O vapor desorption isotherm for Zn-sap. Experimental and calculated XRD patterns are shown as solid red and black lines, respectively. Difference plots are shown at the bottom of the figure as gray lines. The vertical gray bar indicates a modified scale factor for the angle region higher to 10° 2θ compared to the 3-10 °2θ angular range.

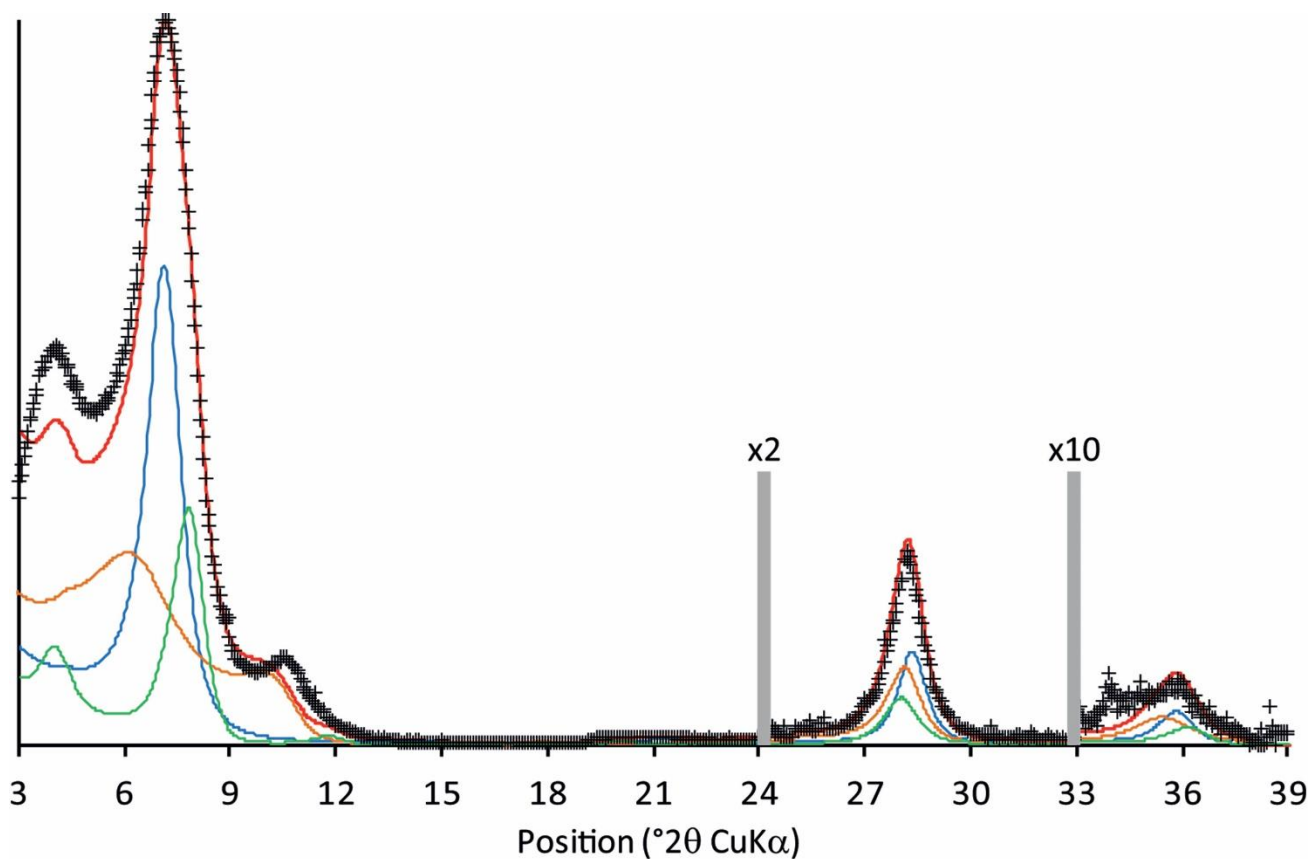


Fig. S15. Respective contributions of the various mixed layers to the diffraction profile calculated for Zn-stev at 55% RH. Mixed layers #1, #2, and #4 (Table S11) are shown as solid orange, blue, and green lines, respectively. Optimum fit and diffraction data are shown as solid red line and black crosses, respectively. The vertical gray bars indicate a modified scale factor for the high-angle regions compared to the 2-24 $^{\circ}2\theta$ range.

Table SI1. Structural parameters used to fit experimental XRD patterns of Zn-stev as a function of relative humidity.

| | %RH | 90 | 85 | 80 | 75 | 70 | 65 | 60 | 55 | 50 | 45 | 40 | 35 | 30 | 25 | 20 | 15 | 10 | 5 | 2 | |
|---|----------------------|-------|-------|-------|-------|-------|-------|-------|-------|-------|-------|-------|-------|-------|-------|-------|-------|-------|-------|-------|------|
| Layer-to-layer distance (in Å) | 2W | 15.80 | 15.77 | 15.73 | 15.69 | 15.66 | 15.63 | 15.58 | 15.55 | | | | | | | | | | | | |
| | 1W | 12.80 | 12.70 | 12.60 | 12.58 | 12.57 | 12.57 | 12.53 | 12.53 | 12.50 | 12.50 | 12.45 | 12.43 | 12.40 | 12.40 | 12.25 | 12.20 | 12.10 | 11.90 | 11.80 | |
| | 0W | 9.75 | 9.75 | 9.75 | 9.75 | 9.75 | 9.75 | 9.75 | 9.75 | 9.75 | 9.75 | 9.75 | 9.75 | 9.75 | 9.75 | 9.75 | 9.75 | 9.75 | 9.75 | 9.75 | 9.75 |
| Number of H ₂ O molecules [per O ₂₀ (OH) ₄] | 2W layers | 10.6 | 10.4 | 10.0 | 10.0 | 9.8 | 9.6 | 9.4 | 9.0 | 8.8 | | | | | | | | | | | |
| | 1W layers | 4.1 | 4.1 | 4.1 | 4.0 | 4.0 | 3.9 | 3.9 | 3.9 | 3.8 | 3.8 | 3.7 | 3.5 | 3.4 | 3.0 | 2.8 | 2.8 | 2.5 | 2.3 | 1.8 | |
| σ_z (in Å) | | 0.22 | 0.20 | 0.22 | 0.20 | 0.20 | 0.20 | 0.22 | 0.18 | 0.18 | 0.18 | 0.18 | 0.18 | 0.20 | 0.18 | 0.15 | 0.15 | 0.15 | 0.15 | 0.15 | |
| σ^* (in °) | | 4.0 | 3.8 | 4.0 | 3.8 | 3.5 | 3.6 | 3.6 | 3.0 | 2.0 | 3.0 | 2.4 | 2.5 | 2.5 | 2.0 | 2.0 | 2.0 | 2.0 | 2.0 | 2.0 | |
| Mixed layer 1 | Ab (%) | 93 | 92 | 79 | 77 | 64 | 48 | 41 | 38 | 3 | 3 | 2 | 2 | 5 | 14 | 20 | 39 | 41 | 53 | 58 | |
| | 2W | 75 | 75 | 75 | 72 | 72 | 65 | 40 | 40 | | | | | | | | | | | | |
| | 1W | | | | | | | | | 15 | 10 | 10 | 2 | 2 | 2 | 2 | 2 | | | | |
| | 0W | 25 | 25 | 25 | 28 | 28 | 35 | 60 | 60 | 85 | 90 | 90 | 98 | 98 | 98 | 98 | 98 | 98 | 100 | 100 | 100 |
| | CSD size (in layers) | 4.0 | 4.0 | 4.0 | 4.0 | 4.0 | 4.0 | 8.0 | 6.0 | 6.0 | 6.0 | 7.0 | 6.0 | 9.0 | 9.0 | 6.0 | 5.0 | 6.0 | 5.5 | 5.0 | 5.5 |
| Mixed layer 2 | Ab (%) | 7 | 8 | 12 | 15 | 27 | 43 | 56 | 42 | 80 | 82 | 80 | 81 | 83 | 81 | 75 | 61 | 59 | 47 | 42 | |
| | 2W | 40 | 30 | 25 | 25 | 25 | 20 | 15 | 5 | | | | | | | | | | | | |
| | 1W | 50 | 60 | 60 | 60 | 60 | 60 | 65 | 75 | 48 | 48 | 44 | 38 | 34 | 30 | 20 | 20 | 20 | 15 | 15 | |
| | 0W | 10 | 10 | 15 | 15 | 15 | 20 | 20 | 20 | 52 | 52 | 56 | 62 | 66 | 70 | 80 | 80 | 80 | 85 | 85 | |
| | CSD size (in layers) | 5.0 | 5.0 | 5.0 | 5.3 | 6.0 | 6.0 | 6.5 | 6.0 | 6.0 | 6.0 | 9.0 | 7.0 | 7.0 | 9.0 | 8.0 | 6.0 | 6.0 | 7.0 | 6.0 | 5.0 |
| Mixed layer 3 | Ab (%) | | | 9 | 8 | 9 | 9 | 3 | | | | | | | | | | | | | |
| | 2W | | | 50 | 45 | 40 | 35 | 15 | | | | | | | | | | | | | |
| | 1W | | | 50 | 55 | 60 | 65 | 35 | | | | | | | | | | | | | |
| | 0W | | | | | | | 50 | | | | | | | | | | | | | |
| | CSD size (in layers) | | | 4.2 | 6.0 | 7.0 | 7.0 | 4.0 | | | | | | | | | | | | | |
| Mixed layer 4 R=1 with maximum possible degree of ordering (MPDO) | Ab (%) | | | | | | | | 21 | 16 | 15 | 18 | 17 | 13 | 5 | | | | | | |
| | 2W | | | | | | | | 50 | 50 | 50 | 50 | 48 | 48 | 40 | | | | | | |
| | 1W | | | | | | | | 50 | 50 | 50 | 50 | 52 | 52 | 60 | | | | | | |
| | CSD size (in layers) | | | | | | | | 5.0 | 5.0 | 5.0 | 5.0 | 7.0 | 9.0 | 6.0 | | | | | | |

Note: Ab.: Relative abundance; CSD: coherent scattering domain; σ_z : fluctuation of the layer-to-layer distance (in Å); σ^* : orientation parameter(in °)

Table S12. Structural parameters used to fit experimental XRD patterns of Zn-*hct* as a function of relative humidity.

| | %RH | 95 | 90 | 85 | 80 | 75 | 70 | 65 | 60 | 55 | 50 | 45 | 40 | 35 | 30 | 25 | 20 | 15 | 10 | 5 |
|---|-----------|-------|-------|-------|-------|-------|-------|-------|-------|-------|-------|-------|-------|-------|-------|-------|-------|-------|-------|-------|
| Layer-to-layer distance (in Å) | 3W | 18.0 | 18.0 | 18.0 | 18.0 | 18.0 | 18.0 | | | | | | | | | | | | | |
| | 2W | 15.88 | 15.80 | 15.74 | 15.70 | 15.67 | 15.62 | 15.60 | 15.56 | 15.55 | 15.52 | 15.50 | 15.48 | 15.47 | 15.46 | 15.45 | 15.43 | 15.42 | 15.40 | 15.38 |
| | 1W | 13.00 | 12.98 | 12.96 | 12.95 | 12.95 | 12.90 | 12.85 | 12.75 | 12.68 | 12.66 | 12.65 | 12.64 | 12.63 | 12.61 | 12.57 | 12.54 | 12.49 | 12.48 | 12.45 |
| | 0W | | | | | | | | | | | | 9.70 | 9.70 | 9.70 | 9.70 | 9.70 | 9.70 | 9.70 | 9.70 |
| Number of H ₂ O molecules [per O ₂₀ (OH) ₄] | 2W layers | 11.4 | 11.2 | 10.2 | 9.8 | 9.6 | 9.4 | 9.4 | 9.2 | 9.0 | 8.8 | 8.0 | 7.8 | 7.8 | 7.8 | 7.6 | 7.6 | 7.2 | 6.6 | 6.0 |
| | 1W layers | 5.6 | 5.6 | 5.5 | 6.0 | 6.0 | 5.9 | 5.8 | 5.7 | 5.6 | 5.4 | 5.3 | 5.2 | 5.1 | 5.0 | 4.6 | 4.2 | 3.6 | 2.8 | 2.3 |
| σ_z (in Å) | | 0.22 | 0.24 | 0.22 | 0.22 | 0.22 | 0.22 | 0.24 | 0.22 | 0.22 | 0.22 | 0.22 | 0.22 | 0.22 | 0.22 | 0.22 | 0.22 | 0.22 | 0.24 | 0.24 |
| σ^* (in °) | | 7.0 | 9.0 | 9.0 | 8.0 | 9.0 | 7.0 | 9.0 | 9.0 | 9.0 | 9.0 | 9.0 | 8.0 | 8.0 | 7.8 | 7.8 | 7.5 | 6.5 | 7.5 | 8.0 |
| CSD size (in layers) | | 4.0 | 4.6 | 4.8 | 5.0 | 5.2 | 4.5 | 4.0 | 4.2 | 4.5 | 4.7 | 5.0 | 5.0 | 5.0 | 5.0 | 5.0 | 5.0 | 6.0 | 9.0 | 9.0 |
| Mixed layer 1 | Ab (%) | 44 | 57 | 48 | 35 | 30 | 42 | 29 | 27 | 24 | 33 | 41 | 32 | 25 | 20 | 21 | 18 | 23 | 33 | 34 |
| | 3W | 7 | 6 | 6 | 6 | 6 | 6 | | | | | | | | | | | | | |
| | 2W | 90 | 90 | 90 | 90 | 88 | 80 | 95 | 80 | 75 | 55 | 48 | 48 | 45 | 45 | 42 | 40 | 38 | 30 | 25 |
| | 1W | 3 | 4 | 4 | 4 | 6 | 14 | 5 | 10 | 5 | 23 | 28 | 28 | 31 | 31 | 31 | 33 | 34 | 35 | 35 |
| | 0W | | | | | | | | 10 | 20 | 22 | 24 | 24 | 24 | 24 | 27 | 27 | 28 | 35 | 40 |
| Mixed layer 2 | Ab (%) | 38 | 24 | 23 | 21 | 20 | 13 | 20 | 36 | 32 | 12 | 3 | 8 | 19 | 20 | 14 | 14 | 15 | 3 | 14 |
| | 3W | 60 | 60 | 45 | 40 | 37 | 35 | | | | | | | | | | | | | |
| | 2W | 40 | 40 | 55 | 60 | 63 | 65 | 5 | 5 | 5 | 10 | | | | | | | | | |
| | 1W | | | | | | | 65 | 65 | 65 | 70 | 75 | 50 | 53 | 45 | 45 | 45 | 45 | 30 | 20 |
| | 0W | | | | | | | 30 | 30 | 30 | 20 | 25 | 50 | 47 | 55 | 55 | 55 | 55 | 70 | 80 |
| Mixed layer 3 | Ab (%) | 18 | 16 | 14 | 15 | 21 | 27 | 51 | 37 | 44 | 54 | 56 | 60 | 55 | 60 | 66 | 68 | 62 | 64 | 52 |
| | 3W | | | | | | | | | | | | | | | | | | | |
| | 2W | 40 | 30 | 25 | 20 | 20 | 15 | 30 | 30 | 20 | 10 | | | | | | | | | |
| | 1W | 60 | 70 | 75 | 80 | 80 | 85 | 65 | 65 | 70 | 68 | 80 | 80 | 80 | 75 | 70 | 65 | 60 | 50 | 45 |
| | 0W | | | | | | | 5 | 5 | 10 | 22 | 20 | 20 | 20 | 25 | 30 | 35 | 40 | 50 | 55 |
| Mixed layer 4 | Ab (%) | | 3 | 15 | 28 | 29 | 17 | | | | | | | | | | | | | |
| | 3W | | | | | | | | | | | | | | | | | | | |
| | 2W | | 68 | 65 | 65 | 60 | 45 | | | | | | | | | | | | | |
| | 1W | | 32 | 35 | 35 | 40 | 55 | | | | | | | | | | | | | |
| | 0W | | | | | | | | | | | | | | | | | | | |

Note: Ab.: Relative abundance; CSD: coherent scattering domain; σ_z : fluctuation of the layer-to-layer distance (in Å); σ^* : orientation parameter(in °)

Table SI3. Structural parameters used to fit experimental XRD patterns of Zn-sap as a function of relative humidity.

| | %RH | 95 | 90 | 85 | 80 | 75 | 70 | 65 | 60 | 55 | 50 | 45 | 40 | 35 | 30 | 25 | 20 | 15 | 10 | 5 |
|---|-----------|-------|-------|-------|-------|-------|-------|-------|-------|-------|-------|-------|-------|-------|-------|-------|-------|-------|-------|-------|
| Layer-to-layer distance (in Å) | 3W | 18.0 | 18.0 | 18.0 | 18.0 | 18.0 | 18.0 | 18.0 | | | | | | | | | | | | |
| | 2W | 15.58 | 15.53 | 15.52 | 15.50 | 15.40 | 15.38 | 15.37 | 15.34 | 15.32 | 15.27 | 15.24 | 15.23 | 15.22 | 15.21 | 15.16 | 15.16 | 15.15 | 15.15 | 15.15 |
| | 1W | 12.82 | 12.81 | 12.80 | 12.80 | 12.80 | 12.80 | 12.79 | 12.78 | 12.74 | 12.70 | 12.60 | 12.55 | 12.55 | 12.55 | 12.50 | 12.46 | 12.38 | 12.29 | 12.24 |
| | 0W | | | | | | | | | | | | 9.70 | 9.70 | 9.70 | 9.70 | 9.70 | 9.70 | 9.70 | 9.70 |
| Number of H ₂ O molecules [per O ₂₀ (OH) ₄] | 2W layers | 11.0 | 10.4 | 10.0 | 9.4 | 8.8 | 8.6 | 8.4 | 8.2 | 8.0 | 8.0 | 7.8 | 7.6 | 7.4 | 7.0 | 6.8 | 6.6 | 6.0 | 4.4 | 4.0 |
| | 1W layers | 5.7 | 5.6 | 5.5 | 5.5 | 5.3 | 5.7 | 5.7 | 5.7 | 5.6 | 5.5 | 5.4 | 5.3 | 5.2 | 5.0 | 4.5 | 4.1 | 3.5 | 3.1 | 2.5 |
| σ_z (in Å) | | 0.22 | 0.22 | 0.22 | 0.22 | 0.22 | 0.21 | 0.18 | 0.18 | 0.17 | 0.17 | 0.19 | 0.21 | 0.24 | 0.22 | 0.22 | 0.22 | 0.22 | 0.22 | 0.20 |
| σ^* (in °) | | 4.0 | 5.0 | 5.0 | 4.8 | 4.5 | 4.2 | 3.6 | 3.4 | 3.2 | 3.0 | 4.0 | 4.0 | 4.6 | 4.6 | 4.3 | 4.6 | 4.6 | 3.8 | 3.8 |
| CSD size (in layers) | | 4.5 | 4.8 | 5.2 | 5.5 | 5.5 | 5.5 | 5.5 | 5.0 | 5.0 | 4.5 | 4.5 | 4.2 | 4.7 | 4.7 | 5.0 | 5.1 | 5.0 | 5.0 | 5.0 |
| Mixed layer 1 | Ab (%) | 48 | 49 | 38 | 39 | 34 | 33 | 28 | 28 | 19 | 21 | 14 | 28 | 21 | 17 | 14 | 10 | 9 | 7 | 5 |
| | 3W | 3 | 2 | 2 | 2 | 2 | 2 | 2 | | | | | | | | | | | | |
| | 2W | 97 | 97 | 97 | 96 | 96 | 96 | 96 | 97 | 96 | 88 | 85 | 74 | 74 | 68 | 68 | 65 | 60 | 60 | 58 |
| | 1W | | 1 | 1 | 2 | 2 | 2 | 2 | 3 | 4 | 12 | 15 | 11 | 11 | 15 | 15 | 18 | 20 | 20 | 20 |
| | 0W | | | | | | | | | | | | 15 | 15 | 17 | 17 | 17 | 20 | 20 | 22 |
| Mixed layer 2 | Ab (%) | 30 | 32 | 32 | 28 | 29 | 25 | 22 | 19 | 15 | 11 | 9 | 7 | 22 | 32 | 30 | 38 | 38 | 40 | 37 |
| | 3W | 50 | 45 | 40 | 40 | 40 | 40 | 40 | 40 | 40 | 40 | 35 | | | | | | | | |
| | 2W | 50 | 55 | 60 | 60 | 60 | 60 | 60 | 60 | 60 | 60 | 65 | 10 | 10 | 8 | | | | | |
| | 1W | | | | | | | | | | | | 60 | 60 | 62 | 65 | 65 | 60 | 55 | 50 |
| | 0W | | | | | | | | | | | | 30 | 30 | 30 | 35 | 35 | 40 | 45 | 50 |
| Mixed layer 3 | Ab (%) | 17 | 13 | 10 | 10 | 12 | 14 | 18 | 17 | 32 | 45 | 46 | 49 | 45 | 48 | 42 | 37 | 42 | 41 | 47 |
| | 3W | 10 | | | | | | | | | | | | | | | | | | |
| | 2W | 20 | 30 | 25 | 20 | 18 | 18 | 18 | 10 | 3 | 3 | 3 | 3 | 3 | 3 | 1 | | | | |
| | 1W | 70 | 70 | 75 | 80 | 82 | 82 | 82 | 90 | 97 | 97 | 97 | 97 | 97 | 97 | 98 | 99 | 96 | 94 | 80 |
| | 0W | | | | | | | | | | | | | | | 1 | 1 | 4 | 6 | 20 |
| Mixed layer 4 | Ab (%) | 5 | 7 | 20 | 23 | 25 | 28 | 32 | 36 | 35 | 23 | 30 | 16 | 12 | 3 | 15 | 15 | 12 | 12 | 11 |
| | 3W | 5 | | | | | | | | | | | | | | | | | | |
| | 2W | 70 | 72 | 72 | 70 | 70 | 65 | 65 | 55 | 55 | 45 | 42 | 25 | 25 | 25 | 25 | 25 | 25 | 25 | 25 |
| | 1W | 25 | 28 | 28 | 30 | 30 | 35 | 35 | 45 | 45 | 55 | 58 | 73 | 73 | 73 | 73 | 73 | 73 | 73 | 73 |
| | 0W | | | | | | | | | | | | 2 | 2 | 2 | 2 | 2 | 2 | 2 | 2 |

Note: Ab.: Relative abundance; CSD: coherent scattering domain; σ_z : fluctuation of the layer-to-layer distance (in Å); σ^* : orientation parameter(in °)